Article

Potential Rockfall Source Identification and Hazard Assessment in High Mountains (Maoyaba Basin) of the Tibetan Plateau

Juanjuan Sun [1,2,3], **Xueliang Wang** [1,2,3,*], **Songfeng Guo** [1,2,3], **Haiyang Liu** [4], **Yu Zou** [1,2,3], **Xianglong Yao** [5], **Xiaolin Huang** [6] **and Shengwen Qi** [1,2,3,*]

1   Key Laboratory of Shale Gas and Geoengineering, Institute of Geology and Geophysics, Chinese Academy of Sciences, Beijing 100029, China; sunjuanjuan17@mails.ucas.ac.cn (J.S.)
2   Institutions of Earth Science, Chinese Academy of Sciences, Beijing 100029, China
3   University of Chinese Academy of Sciences, Beijing 100049, China
4   China Aero Geophysical Survey and Remote Sensing Center for Natural Resources, Beijing 100083, China
5   China Three Gorges Corporation Science and Technology Research Institute, Beijing 101199, China
6   Department of Civil Engineering, School of Human Settlements and Civil Engineering, Xi'an Jiaotong University, Xianning West Road No. 28, Xi'an 710049, China
*   Correspondence: wangxueliang@mail.iggcas.ac.cn (X.W.); qishengwen@mail.iggcas.ac.cn (S.Q.)

Abstract: Potential rockfall source areas are widely distributed in the high mountain areas of the Tibetan Plateau, posing significant hazards to human lives, infrastructures, and lifeline facilities. In a combination of field investigation, high-precision aerial photogrammetry, and numerical simulation, we took the Maoyaba basin as an example to explore a rapid identification method for high-altitude rockfall sources. An automatic potential rockfall source identification (PRSI) procedure was introduced to simplify the process of rockfall source identification. The study revealed that rockfall sources are concentrated in areas with intense frost weathering. Our identification results were validated using rockfall inventory data detection from remote sensing images and field investigation. Of the rockfall source areas identified by the PRSI procedure, 80.85% overlapped with the remote sensing images result. The accuracy assessment using precision, recall, and F1 score was 0.91, 0.81, and 0.85, respectively, which validates the reliability and effectiveness of the PRSI procedure. Meanwhile, we compared the rockfall source distribution of five DEMs with different resolutions and four neighborhood areas. We discovered that, in addition to high-resolution DEMs (i.e., 1 m and 2 m), medium-resolution DEMs (i.e., 5 m, 12.5 m) also perform well in identifying rockfall sources. Finally, we conducted a hazard assessment based on Culmann's two-dimensional slope stability model and rockfall hazard vector method. Appropriate protective measures should be taken at high-hazard sections to safeguard pedestrians, vehicles, and related infrastructure from rockfalls.

Keywords: high mountains; potential rockfall source identification; hazard assessment; DEM resolution

1. Introduction

Rockfall refers to the dynamic process of blocks moving rapidly down a slope through free fall, impact rebound, projectile movement, rolling, or sliding and finally accumulating in a relatively gentle area or near an obstacle [1,2]. It is a common type of mass movement that poses significant threats to human lives and property in mountainous areas. Rockfalls are characterized by their high concealment, sudden detachment, strong continuity, and high energy, with volumes ranging from a few cubic centimeters to thousands of cubic meters [3,4]. Considerable research has been conducted worldwide on rockfall hazards, including rockfall source area identification, rockfall trajectory simulation, rockfall velocity and energy evaluation, and risk analysis. In particular, the uncertainty in potential source area distribution makes rockfall hazard assessment a complex task [5]. Therefore, the quest to identify rockfall source areas has captured the attention and interest of many scientists [6–8].

Rockfall sources can be carefully studied through in situ investigation or a rockfall inventory dataset [9]. However, the traditional field investigation method consumes much more time and human resources when conducted at the regional scale. Meanwhile, in situ and inventory data are usually unavailable in the high mountain regions of the Tibetan Plateau [10]. The availability of high-resolution digital elevation models (DEM) and 3D surface landscape models has enabled the development of approaches for identifying rockfall sources [11,12].

Some researchers identified rockfall sources at a regional scale by utilizing remote sensing interpretation technologies, such as multi-temporal aerial images, high-resolution LiDAR point clouds, and DEMs [13–15]. Additionally, machine learning techniques have become a popular approach to assess rockfall issues, requiring large-scale sample training [5,14–17]. Alternatively, unstable rock areas can be identified through the slope-angle threshold, considering the high probability of rockfall occurrence in steep slopes [8,16–18]. For example, Michoud et al. (2012) conducted a detailed slope-angle analysis of a high-resolution DEM to detect potential rockfall source areas, taking into account the normal distributions of cliff units. Lopez-Saez et al. (2016) established a fixed threshold slope angle of 49° to identify source areas. Mote et al. (2019) suggested that continuous cliff bands with slopes steeper than 45° could be used as a criterion for identifying source areas. However, the aforementioned three methods have their limitations, such as being time consuming, requiring large sample sizes, and disregarding other contributing factors [19]. Therefore, this study focuses on using analysis methods to evaluate the slope stability against rotational failure. The classical Culmann's model assumes a wedge failure mechanism, which is reasonable in the presence of a planar discontinuity or weakness zone in the rock mass [20–22]. Wang et al. (2021) proposed a new approach to identify rockfall source areas, combining the relief and slope angles [23]. Based on previous studies, a potential rockfall source identification (PRSI) procedure based on Culmann's model and the ArcGIS framework was developed to automatically identify the rockfall source area in this study.

Additionally, in recent decades, rockfall hazard assessment has greatly improved due to the increasing availability of high-resolution DEMs and their combination with 3D simulation models and GIS platforms [4,24,25]. It is convenient to model rock mass movement with a detailed trajectory, which supports a high level of geomorphological mapping and hazard assessment [15,16,26].

In this study, we developed a procedure of PRSI and clarified the impact of various factors on the identification results. Additionally, we conducted rockfall hazard assessments in the high mountains of the Tibetan Plateau. The Maoyaba basin, characterized by steep slope, complex geological conditions, and frequent rockfalls, provided an exceptional opportunity to verify the reliability and effectiveness of the PRSI procedure. This is because, in this open and vegetation-free high mountain area, the PRSI procedure could be used in conjunction with remote sensing images to identify rockfall sources simultaneously. The research objectives of this study were as follows: (1) Develop a PRSI procedure which is based on the ArcGIS framework and Culmann's two-dimensional slope stability model. This procedure was combined with field investigation and aerial photogrammetry to achieve a more accurate and rapid identification of slope instability on a regional scale. (2) Analyze the effects of DEM resolution and neighborhood area on potential rockfall source identification results. (3) Predict potential rockfall trajectories and conduct hazard assessment.

2. Methods

In order to understand the potential rockfall source identification and the hazard zonation of Maoyaba basin, we performed UAV and field data acquisition, source area identification, and rockfall hazard assessment. The major steps of the adopted approach are illustrated as follows (Figure 1).
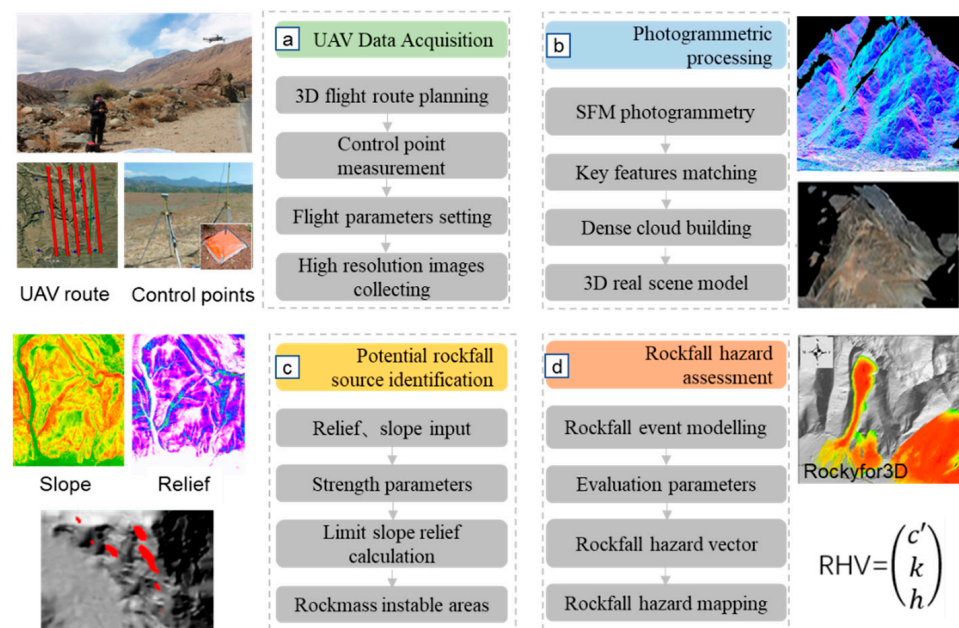
Figure 1. The flowchart of the proposed methodology includes four parts: UAV data acquisition, photogrammetric processing, potential rockfall source identification, and rockfall hazard assessment.

2.1. UAV and Field Data Acquisition

The fieldwork for the rockfall investigation included high-precision mapping and source area verification. Unmanned aerial vehicles (UAV, FEIMA V10, http://www. feimarobotics.com/zhcn/productDetailV10, accessed on April 2019) were used for aerial photography to obtain a 3D dense point cloud, real scene model, and high-precision digital orthophoto map (0.05 m × 0.05 m resolution) [25,27]. It involved several specific steps, including the collection of flight design data, aerial photography, image control measurements, aerial triangulation, and process modeling [27]. The UAV FEIMA V10 was equipped with a DV-LiDAR 22 module, which possesses a 35.9 mm × 24 mm sensor, 18 mm focal lengths, and a wavelength of 1550 nm. During the photogrammetry work, we comprehensively considered the topographic and geomorphic characteristics of the measured area, as well as the performance of the digital camera (focal length, picture frame) and the product scale size when planning the flight path. To meet the data resolution requirements, we ensured that the aerial photography UAV had a heading overlap ratio of more than 80% and a lateral overlap ratio of more than 60%. The structure-from-motion algorithm was used to derive DTM data with a 1 m resolution from overlapping images (with a resolution of 42 million pixels), including feature point extraction, image matching, and bundle adjustment. During the modeling process, we utilized SmartMap software and selected high accuracy with a key point limit of 40,000, aggressive depth filtering, and arbitrary surface type. Moreover, to ensure sample database integrity and data reliability, we combined manual investigation and image analysis methods to describe the characteristics of the hazardous rock.

2.2. Source Area Identification

Rock mass strength is considered as the fundamental controlling factor for slope stability [20,28]. According to Culmann's two-dimensional slope stability model (Equation (1)), if the slope relief in the specified neighborhood exceeds the threshold value, then the neighborhood is considered a rockfall-vulnerable area [6,14,29,30]. The procedure of PRSI is as follows (Figure 2).
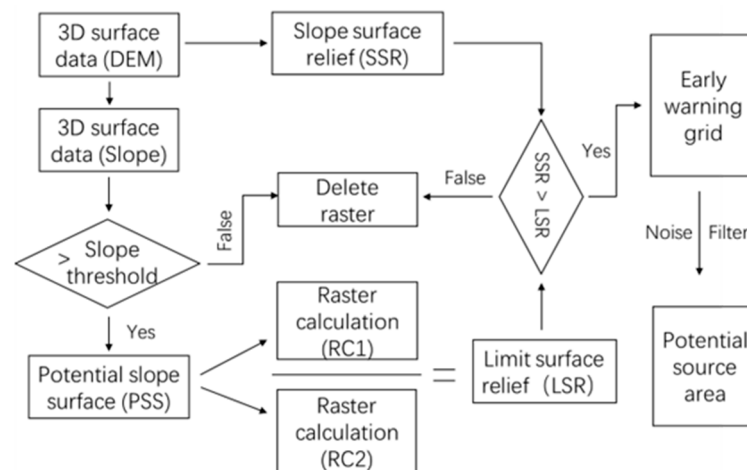
Figure 2. Flow diagram illustrating the potential rockfall source identification procedure.

Based on the 3D surface elevation data (DEM) of the study area, the slope surface relief (SSR) in the neighborhood area (NA) is calculated. The neighborhood area refers to the area of the SSR sampling windows, which is equal to the square of the length of a side. Then, the slope threshold value is assigned based on statistics research. If the gradient of a grid is greater than the threshold value, it is classified as a potential source grid; otherwise, it is classified as a safety grid. Next, the rock mass strength parameters (C, φ) of the bedrock slope at landscape scale are back-calculated. Culmann's model is used to obtain the limit slope relief (LSR) in the NA by raster calculation (Equation (1)) [21,30,31].

The stability state is estimated by comparing the current slope surface relief (SSR) with the limited slope relief (LSR). When SSR > LSR, the corresponding grid is classified as an early warning grid. The potential source area is delineated by filtering noise from the early warning grid. We integrated every step of the procedure based on the ArcGIS platform with a user-friendly interface that allows users to complete identifications within several minutes for tens of square kilometer areas.

$$LSR = \frac{4C}{\rho g} \times \frac{\sin\beta\cos\varphi}{[1 - \cos(\beta - \varphi)]} \tag{1}$$

where LSR is limit slope relief, β is slope angle, ρ is rock density, g is gravitational acceleration, C is cohesion, and φ is friction angle.

2.3. Rockfall Hazard Assessment

In this paper, the rockfall hazard index (RHI) was utilized for hazard assessment, which is a function of three equally important indicators [4]. One of these indicators is probability, and the other two are kinematic parameters [4,32]. Three factors (block number C, kinetic energy K, and jump height H) were selected to categorize the hazard of the study area into three levels: high (I), medium (II), low (III).

The magnitude of the evaluation parameters obtained by numerical simulation was not uniform. To facilitate the superposition of these evaluation parameters and obtain the normalized RHI (Equation (2)), appropriate discontinuity points were selected to reclassify the above parameters into three levels (Table 1). Crosta et al. suggested that a certain part of the slope is dangerous until at least five or more blocks have been simulated to pass through it. Since the number of releasing blocks was multiplied by 100 in the numerical simulation, the number of blocks after normalization was calculated using Equation (3). The reclassification breakpoints were set to 0.2 and 1. The reclassification breakpoints for the bounce height and kinetic energy of the rockfall block were mainly determined based on the protection capacity of existing protective measures, including flexible and rigid protection facilities. Currently, the actual height of flexible protective nets and rockfall barrier dams is about 5–7 m and 10 m, respectively. The maximum protection level for

flexible protective nets can reach around 2500 kJ while that for rockfall barrier dams can reach around 40,000 kJ [33,34]. Therefore, breakpoints of 5 m and 10 m were selected for the block bounce height, while breakpoints of 2500 kJ and 40,000 kJ were chosen for energy.

$$RHI = (C, K, H) \tag{2}$$

$$c = C/(5 \times n) \tag{3}$$

Table 1. The discontinuity points of normalized number, kinetic energy, and jump height.

Number c (Normalized)	c'	Energy K (kJ)	k	Height H (m)	h
<0.2	1	≤2500	1	≤5	1
0.2–1	2	2500–40,000	2	5–10	2
>1	3	≥40,000	3	≥10	3

Here, RHI represents the rockfall hazard index, including block number C, kinetic energy K, and jump height H. The number of rockfall blocks that pass through a grid is normalized using Equation (4), where c represents the actual number of blocks passing through a grid, and n represents the total number of blocks released from each source grid.

$$RHV = \begin{pmatrix} c' \\ k \\ h \end{pmatrix} \tag{4}$$

$$|RH\,V| = \sqrt{(c')^2 + k^2 + h^2} \tag{5}$$

where RHV represents the rockfall hazard vector, c′, k, and h are the values after reclassification of the number, kinetic energy, and jump height of the blocks passing through a certain grid. The reclassification thresholds of normalized block number c, kinetic energy K, and jump height H are shown in Table 1.

Finally, the rockfall hazard vector (RHV) value of each grid cell was calculated, and its modulus was used to perform the hazard assessment. Based on ArcGIS platform, three raster layers were calculated using a raster calculator. Combined with historical rockfall events, the rockfall hazard assessment results were classified into three levels: low level III (1.732, 3), medium level II (3, 4.123), and high level I (4.123, 5.196).

3. Study Area

The Maoyaba basin is located about 30 km to the west of Litang County of the Ganzi Prefecture (Figure 3). The study area is characterized by steep terrain, complex and variable rock structures, and sparse vegetation. Affected by the Litang–Yidun fault belt, rockfall occurs frequently [35,36]. The National Road G318 runs from east to west about 500 m away from the foot of the north mountain, and the potential rockfall disaster impact range requires further prediction and analysis. The study area mainly comprises the Middle and Upper Triassic Tumgou Formation (T₃t), Triassic biotite monzogranite, and Quaternary loose deposits. The Triassic biotite monzonite granite is grayish white and consists of phenocrystalline and matrix. It has a massive structure, and some parts exhibit a streamlined structure formed by phenocrystalline orientation. The Quaternary loose deposits are mainly composed of alluvium, moraine, ice-water deposits, and rockfall deposits. Among them, the moraine, ice-water deposits, and rockfall deposits are not integrated on the granite. They mainly consist of medium sand, boulders, and breccia gravel layers with poor grinding properties (Figure 3).
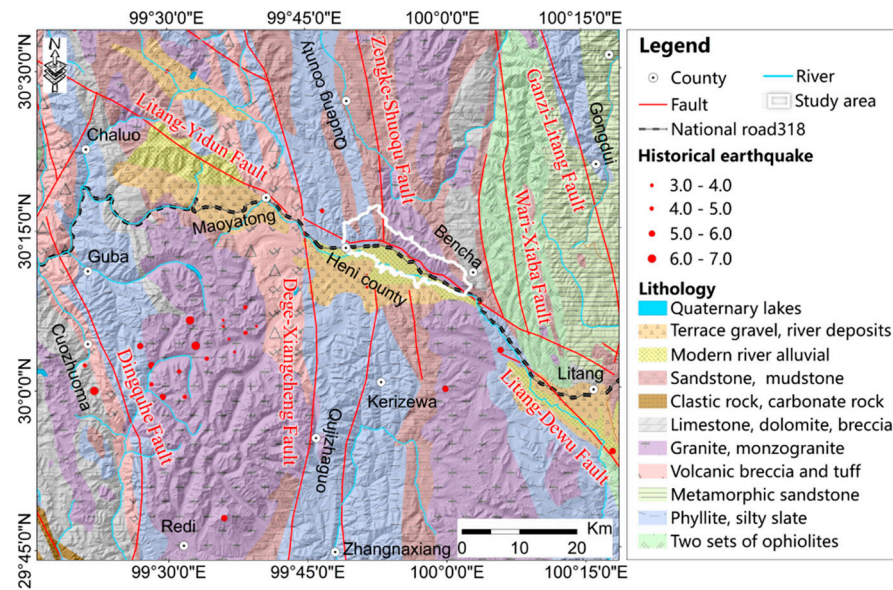
Figure 3. Location and geologic map of the study site. (Shaded relief map based on 12.5 m DEM (Dataset: jaxa/meti alos palsar l1.0 2007). Accessed through ASF DAAC, https://search.asf.alaska.edu).

The Litang–Yidun fault passes through the toe of the slope at the north mountain where the hanging wall on the northeast side is the uplift area, and the footwall on the southwest side is the subsidence area (Figure 4). The overall strike is about 120°. The active fault cuts through the mountains, water systems, and Quaternary sediments, causing the mountain on the north side to rise continuously, forming a steep mountain. The north mountains rise more than 5000 m in height, while the south mountain is generally lower than 4500 m due to weak fault activity signs [35]. Due to the influence of active faults, the north side of Maoyaba exhibits a high degree of ground fault depression, resulting in erosion by the Wuwang River towards the north bank. In contrast, the south bank is characterized by the distribution of large amounts of river alluvial and diluvial materials (Figure 4).
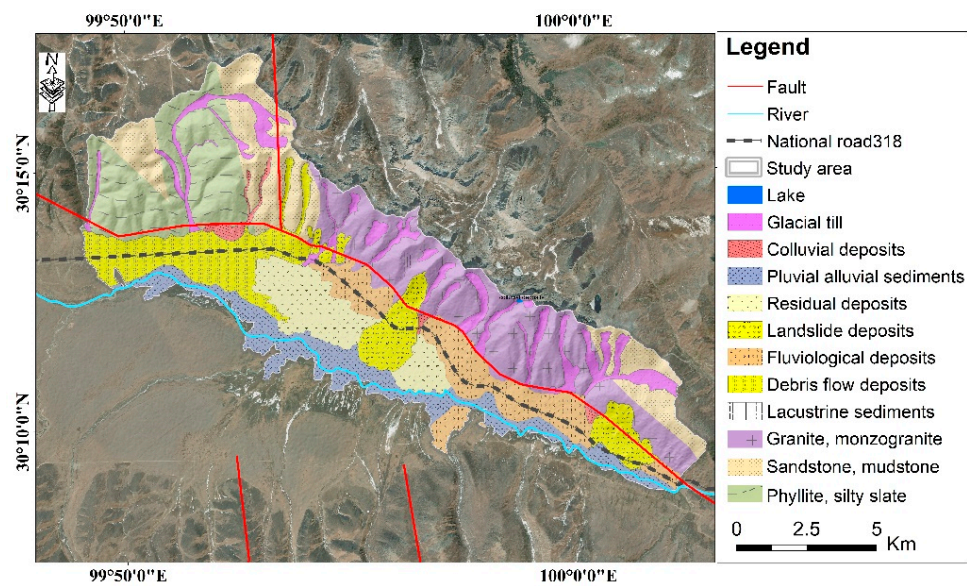

Figure 4. The landscape view and engineering geological map of the Maoyaba basin (the engineering geological map was compiled from field investigation and aerial photogrammetric images).

The study area is part of a huge mountainous region characterized by strong ultraviolet radiation, significant temperature differences between day and night, and significant seasonal temperature variations. The annual maximum temperature can reach above

50 °C, while the annual minimum temperature is approximately −30.6 °C. Repeated frost weathering causes the exposed rock mass to gradually become loose and broken, resulting in poor slope stability. Due to the deterioration of the slope rock mass under the action of strong freezing erosion, rockfall disasters occur frequently.

4. Results and Analysis

4.1. Potential Rockfall Source Identification

The raster could be transformed into the source areas by performing the efficient thresholds of slope angle and relief, derived from the raster calculation. Figure 5 illustrates the main morphological units in the Maoyaba basin classified by slope angle and relief. Based on the obtained threshold (Equation (1)), the limited slope-relief raster was intersected with the slope-angle raster within the GIS environment to create probable rockfall source regions. Subsequently, the area could be identified as a potential rockfall source area if its present relief exceeded the limit relief corresponding to its slope angle based on the PRSI procedure.
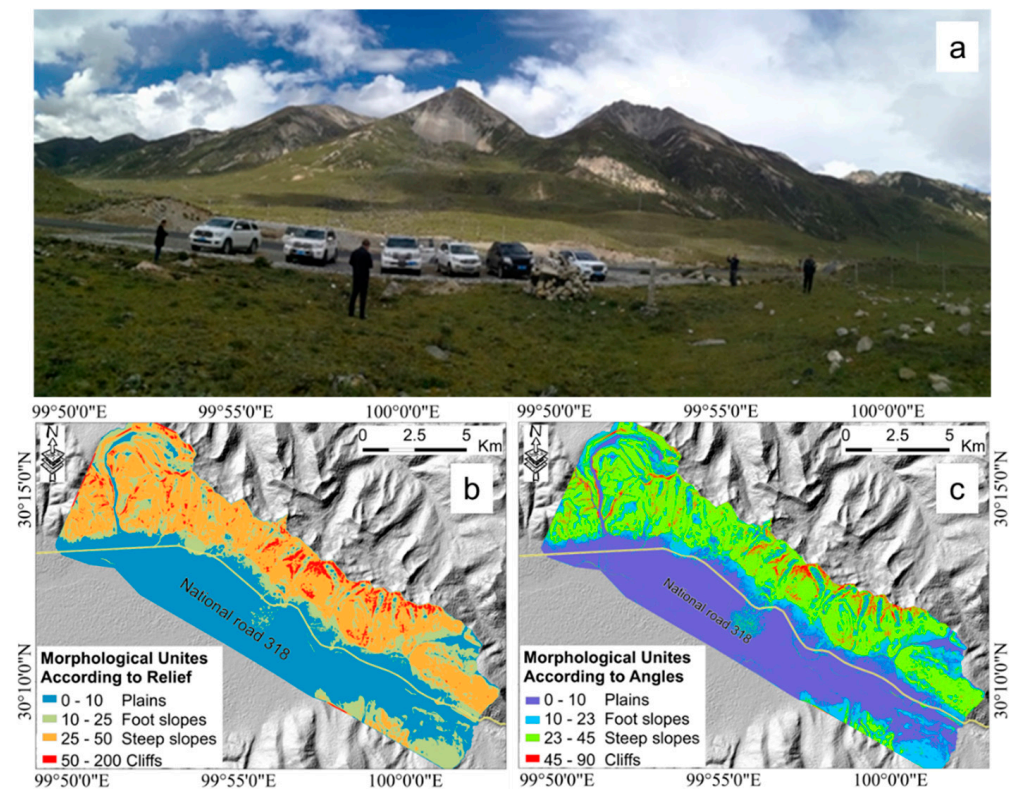

Figure 5. Example of wide-angle photographs in the field (**a**) and main morphological units in the Maoyaba basin according to slope angle (**b**) and relief (**c**) (shaded relief map based on 1 m DEM, accessed through UAV photogrammetry).

The parameters assumed in the identification of rockfall source areas are shown in Table 2. According to the historical data and reference, rockfalls generally do not occur when the slope angle is less than 15°. Therefore, we chose 15° as the slope threshold value. Regarding the neighborhood area value, we discuss it in the discussion part. Additionally, the strength parameters c and φ were fitted by historical rock scars data according to Culmann's model. The historical sites were located in the Wolong region in the Tibetan Plateau. The lithology of the area is mainly diorite and granite with a small component of phyllite, which is similar to the lithology of Maoyaba region.

Table 2. Values of the parameters assumed in rockfall source area identification.

Parameters	Symbol	Unit	Value	Comment
Slope threshold value	S_t	°	15	History rockfalls statistic
Neighborhood area	NA	m	200	
Slope surface relief	SSR	m	Hmax–Hmin	According to DEM calculation
Limit surface relief	LSR	m	$\frac{4C}{\rho g} \times \frac{\sin\beta\cos\varphi}{[1-\cos(\beta-\varphi)]}$	Culmann's two-dimensional slope stability model
Coherent coefficient	c	kPa	240	History rockfalls fitting
Friction coefficient	φ	°	23	History rockfalls fitting
Rock density	ρ	kg/m^3	2800	Constant term
Gravitational acceleration	g	m/s^2	9.8	Constant term

Most of the rockfall source areas are distributed at the upper-top part and the lower parts of the slope, where slope angles are relatively steeper. This distribution is likely to be affected by the intense fault incision and frost weathering (Figure 6). The slope angle, relief, elevation, and the distance from the G318 for all the vulnerable grids were analyzed, and their frequency distributions were obtained. According to the results (Figure 7a), the rockfall source areas prefer to distribute on slopes with angles ranging from 55° to 75°. The relief of the vulnerable areas ranges from 160 m to 240 m (Figure 7b). Based on the distribution statistics of elevation (Figure 7c), the rockfall sources in the study area exhibit a normal distribution, especially concentrated in areas with intense frost weathering. Additionally, most of the source grids are distributed at distances ranging from 800 m to 5000 m away from the National Road G318 (Figure 7d).
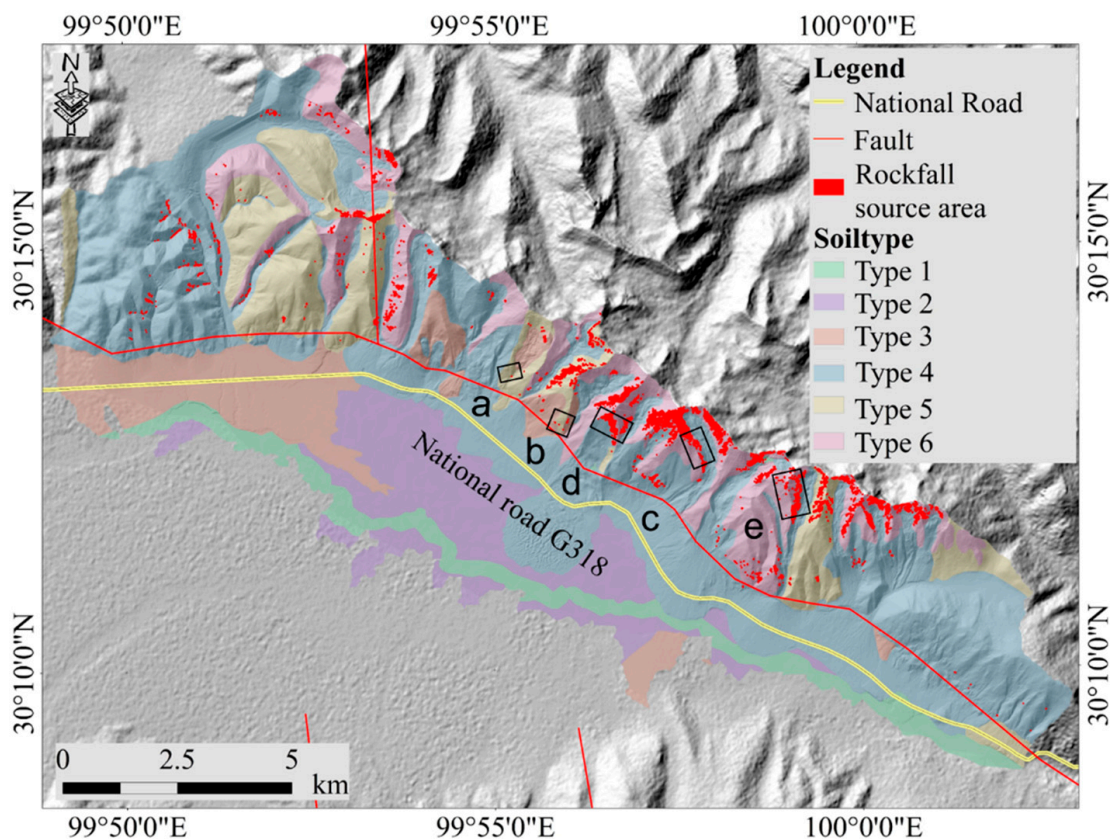

Figure 6. Identification results of rockfall source and classification of soil types in the study area (the polygons with labels a to e indicate the locations of field validation points; shaded relief map based on 1 m DEM, accessed through UAV photogrammetry).
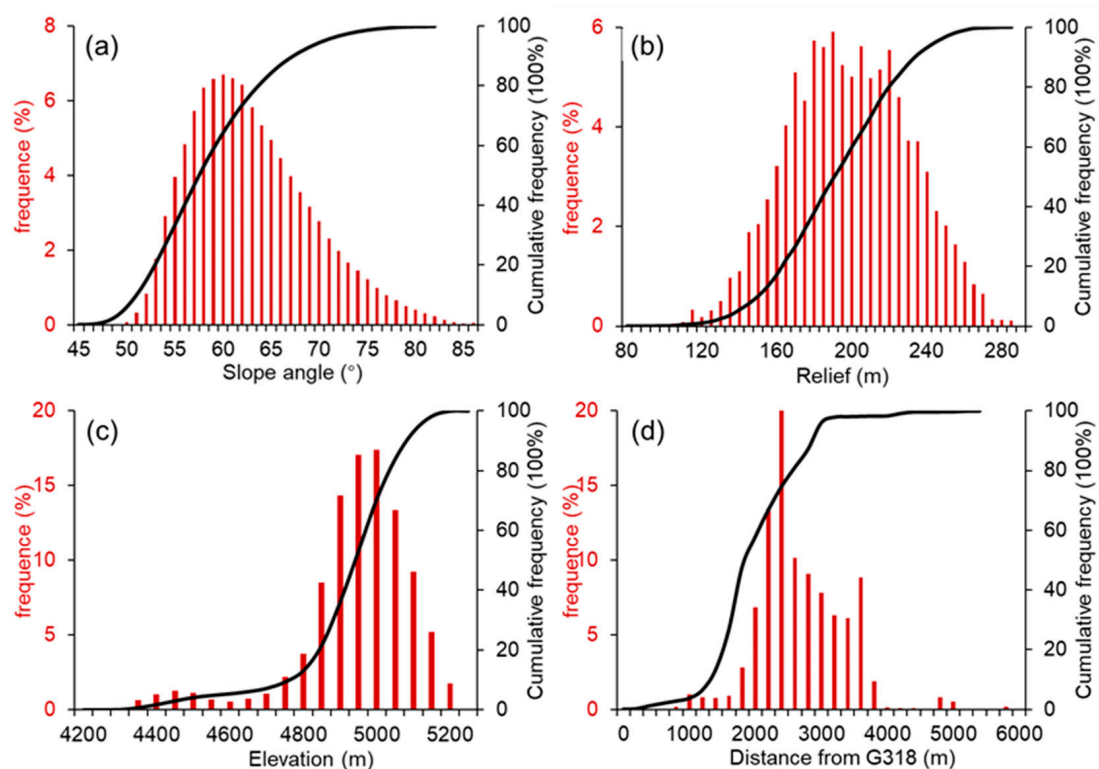
Figure 7. The distribution of slope, relief, elevation, and distance of the identified rockfall source areas within different susceptibility classes. (**a**) the distribution of slope angle; (**b**) the distribution of relief; (**c**) the distribution of elevation; (**d**) the distribution of distance from national road G318.

4.2. Validation

4.2.1. Potential Rockfall Source Identification by Remote Sensing Images

Proper validation should be based on the comparison between the prediction results and actual observations. The Maoyaba basin is characterized by an open landscape with sparse vegetation. This unique feature provides an exceptional opportunity to identify rockfall source area using remote sensing images. Therefore, we compared the differences between the two methods to validate the prediction results.

The composite figure presents the identification results of the PRSI procedure and remote sensing images, as well as the magnified comparison of four local areas (Figure 8). There was an 80.85% overlap between rockfall source areas identified by the PRSI procedure and the results obtained using remote sensing images. Furthermore, the accuracy assessment of the developed PRSI procedure indicates that the model can efficiently identify potential rockfall source areas with a precision, recall score, and F1 score of 0.91, 0.81, and 0.85, respectively. The magnified views provide a more intuitive display of the characteristics of the two identification methods (Figure 8a–d). Obviously, both methods identified locations where historical rockfalls occurred. Compared to the spatially generalized remote sensing identification, the PRSI procedure is more detailed and can identify more hazardous blocks in a specific area. This facilitates the adoption of targeted mitigation measures.

4.2.2. Field Investigation

Most of the rockfall source areas identified by the PRSI procedure are distributed on slopes with high relief and steep terrain (Figure 7). This observation of rockfall distribution in the field is consistent with the findings from the PRSI procedure (Figure 9). Most of the historical rockfall deposits are distributed at the foot of slopes with identified rockfall source areas, indicating that the identified rockfall source areas are associated with historical rockfalls. This suggests that unstable slopes in these areas are prone to future rockfall events.
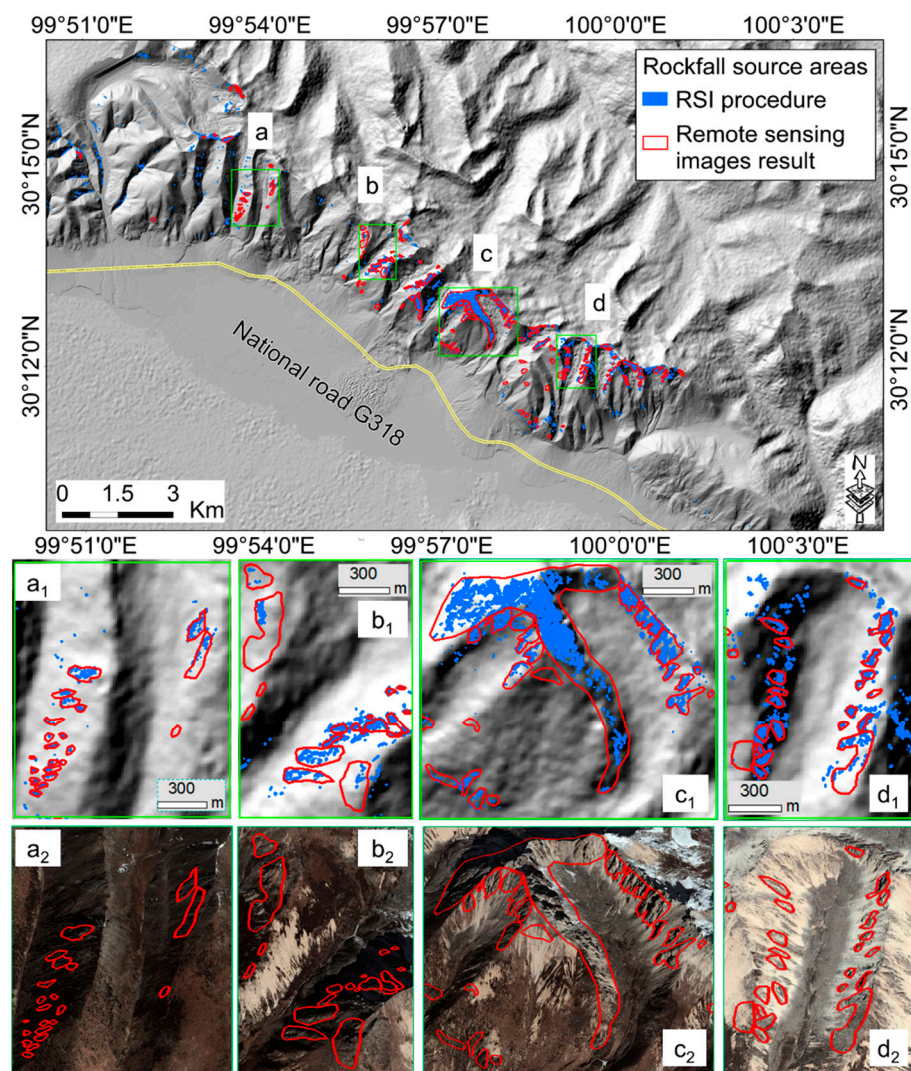
Figure 8. Potential rockfall source identification by PRSI (a_1–d_1) and remote sensing images (a_2–d_2). The blue color represents the identification result of PRSI procedure. The red color represents the identification result of remote sensing images (shaded relief map based on 1 m DEM, accessed through UAV photogrammetry).

We found that three dominant structures exist within the rock mass, construct structure J1, N6~25°E/41°~50°; construct structure J2, S2°~26°W/45°~68°; and unloading structure J3, N56°~78°W/60°~76° (Figure 9). At the location where the fault passes through, the rock undergoes strong destruction and deformation, resulting in clear cutting of structural planes (Figure 9a,b). This leads to a discontinuous, fragmented, and loose rock mass. Furthermore, the development of structural planes is more pronounced in high-altitude areas due to frost weathering. This results in loose and fragile rock masses that have a widespread distribution of rockfall source areas (Figure 9c–e). The consistency between the PRSI and field investigation results further demonstrate the reliability of the method.

4.3. Rockfall Hazard Assessment

4.3.1. Back Analysis of Simulation Parameters

The occurrence of dangerous rocks in this area is mainly controlled by faults and frost weathering. Faults control the development of dominant joints, and frost weathering accelerates the deterioration of rock mass quality. The dangerous rock has an angular shape, so the rock shape was set as a cuboid (bl shape value was 1). Then, based on the field investigation and UAV aerial photogrammetry image data, slope materials were classified

into six categories, exposed bedrock area, bedrock area covered by a thin weathering layer, debris slope, rock debris accumulation slope, fine soil material area, and river or swamp area (Figure 6). The values for soil type were 6, 5, 4, 3, 2, and 1, respectively. This indicates that the decrease in rock and soil elasticity is directly related to the normal recovery coefficient Rn (Table 3).
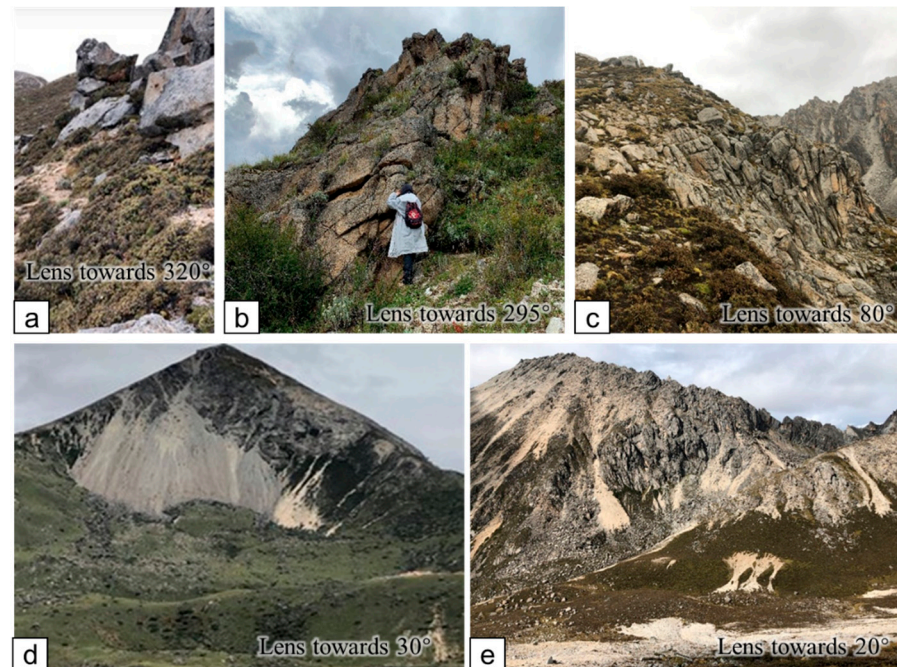

Figure 9. Field validation of the identified rockfall source area (the location of each sub-picture is shown in Figure 6).

Table 3. Numerical simulation parameters of slope materials in study area.

Underground Description	Rn Value Range	Mean Rn Value	Rg70, rg20, rg10	Soil Type
Bedrock	0.48–0.58	0.53	0, 0, 0.05	6
Bedrock with thin weathered material or soil cover bedrock	0.39–0.47	0.43	0, 0.05, 0.1	5
Talus slope (Ø > 10 cm) or compact soil with large rock fragments	0.34–0.42	0.38	0.05, 0.1, 0.2	4
Scree (Ø < 10 cm) or medium-compact soil with small rock fragments or forest road	0.30–0.36	0.33	0.03, 0.05, 0.05	3
Fine soil material	0.21–0.25	0.23	0, 0, 0	2
River, swamp, or material in which a rock could penetrate completely	0	0	100, 100, 100	1

To improve the accuracy and reliability of the numerical results, five historical rockfalls with clear sources and obvious deposits were selected as back analysis sites to invert the slope material parameters before simulation (Figure 10). There were 3709, 3956, 6441, 1132, and 1250 grids in the five inversion source areas, respectively. The calculation was set 100 times, that is, 3.71×10^5, 3.96×10^5, 6.44×10^5, 1.13×10^5, and 1.25×10^5 blocks were thrown. In addition, the rg70, rg20, and rg10 values of different slope materials were repeatedly adjusted until the simulated blocks from the source area were deposited within the current deposit range (Table 3). These three values represent the slope surface roughness, ranging from 0 m to 100 m. The surface roughness is used to calculate the tangential coefficient of restitution. Therefore, it is just a parameter that determines energy

loss during a rebound on the surface; it is not a roughness that is added to the topography as represented by the DEM.
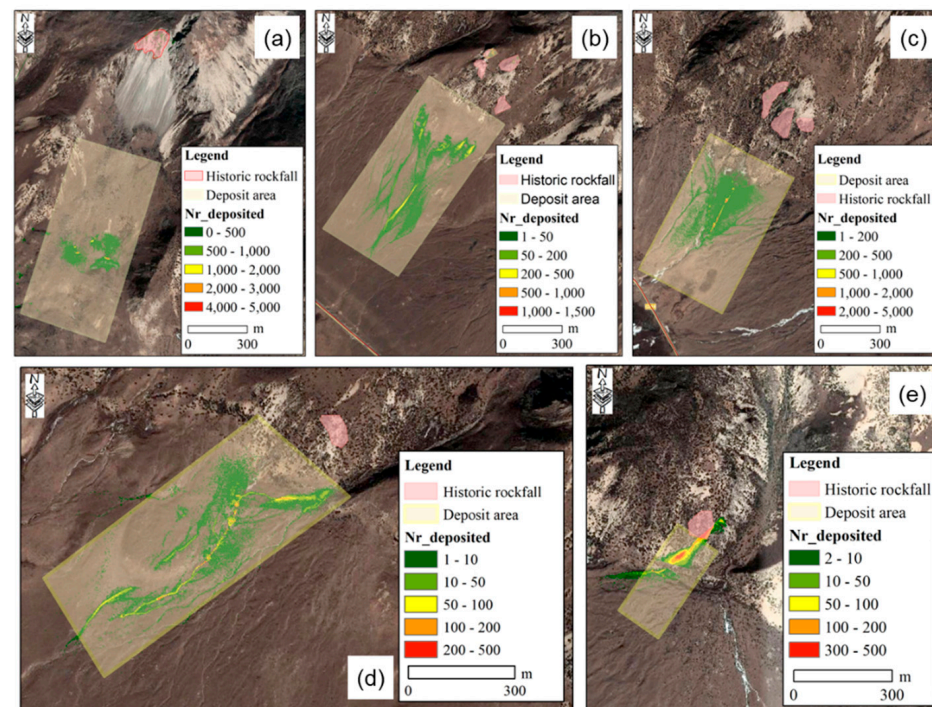

Figure 10. Back analysis of simulation parameters. (**a**–**e**) Five historical rockfalls with clear sources and obvious deposits.

We used an index A to evaluate the inversion accuracy (Equation (6)). The calculation results showed that the number of blocks deposited in the accumulation area was 3.59×10^5, 3.77×10^5, 6.339×10^5, 1.10×10^5, and 0.992×10^5, respectively (Equation (6)), and the corresponding accuracy rates were 96.77%, 95.20%, 98%, 97.35%, and 73.60%, respectively, indicating that the slope parameter is reasonable. The average values of slope material parameters of the five sites were selected as the final simulation parameters.

$$A = \frac{N_d}{N_{Total}} \tag{6}$$

where N_d is the number of stagnant blocks in the grid of the deposition area, and N_{total} is the total number of released blocks.

4.3.2. Rockfall Hazard Assessment

Based on the obtained potential rockfall source area and slope parameters, the 3D numerical simulation of the dangerous blocks was carried out. In the simulation, each source grid released blocks 100 times, and parameters such as block velocity, energy change, and final deposition position were calculated (Figure 11).

The jump height, velocity, energy, arrival probability, and deposition blocks of dangerous rocks after instability are shown in Figure 11. The potentially dangerous rock moves down the slope after instability, with a speed up to 50 m/s (Figure 11a). Due to the sharp steepening of the terrain, the jump height can reach 20 m (Figure 11b), and the energy of a falling block can reach up to 3×10^5 KJ (Figure 11c). We represented the hazard zone of potential rockfall by the probability of unstable blocks reaching each grid (Figure 11d). There is a small probability that the potential rockfall blocks will move onto National Highway G318, posing a threat to passing vehicles or pedestrians.
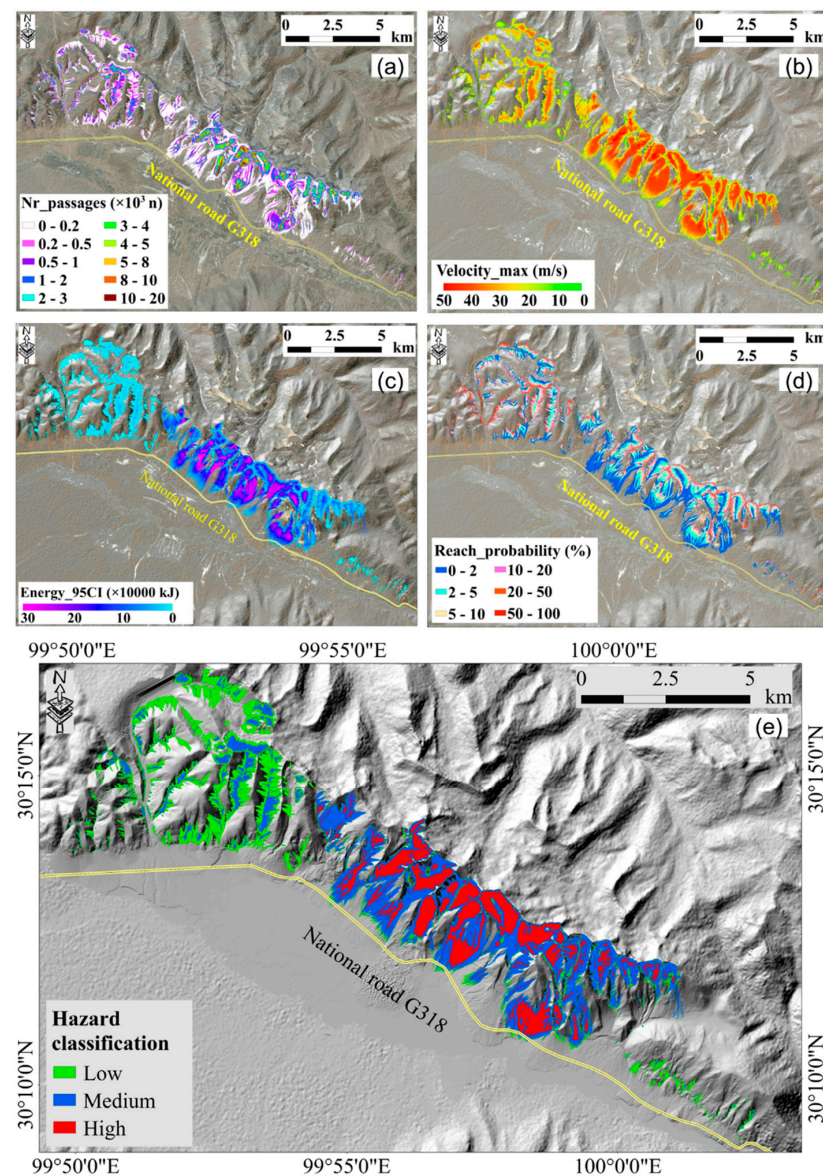
Figure 11. Numerical simulation results of potential blocks' movement characteristics in the study area. (**a**) The number of blocks passing through each cell; (**b**) the absolute maximum simulated velocity per raster cell; (**c**) kinetic energy of blocks passing through each cell; (**d**) distribution characteristics of blocks' reach probability; (**e**) hazard assessment map of study area (shaded relief map based on 1 m DEM, accessed through UAV photogrammetry).

According to the hazard zoning results, the areas of high, medium, and low hazard are 12 km², 9.25 km², and 8.73 km², respectively (Figure 11e). The maximum travel distance of the rock is 3.83 km, 300 m south of National Highway G318. Part of National Highway G318 passes through the low-hazard area. According to the simulation results, pedestrians, vehicles, and related infrastructure are at risk of being affected by rockfalls, and appropriate protective measures should be taken.

5. Discussion

Our new procedure provides a feasible solution for the rapid identification of rockfall source areas, which is essential for hazard assessment and disaster prevention and mitigation. There are several issues to pay special attention to when applying it, as they can lead to uncertainty in the results.

The accuracy of the identification results heavily depends on the resolution of the DEM since it provides fundamental data for analysis [37,38]. In addition to recording spatial elevation information, the DEM also serves as the primary data source for deriving other important geomorphic parameters such as slope and relief [23,38]. Therefore, selecting the appropriate resolution of DEM is crucial to ensuring accurate predictions and reliable analyses of geographical phenomena. In general, increasing the resolution of a DEM leads to more precise values for relief and slope angles of historical rockfalls, as well as the potential rockfall source areas [37,39,40]. However, acquiring a high-quality DEM at a regional scale poses a significant financial expense currently.

We calculated the results for five different resolutions to qualitatively compare the influence of DEM resolution on rockfall source area identification (Figure 12a). From the perspective of the source areas spatial distribution, the identification results at low resolutions were not ideal. We calculated the source area identified using DEMs with different resolutions. When compared to the identification result using a 1 m DEM as a reference, we found that DEMs with resolutions of 2 m, 5 m, 12.5 m, and 30 m were able to identify 94%, 73%, 60%, and 16% of the source areas, respectively. The identification results for rockfall sources using the 1 m and 2 m DEM resolutions were the best (Figure 12b,c), followed by the results from DEMs with resolutions of 5 m and 12.5 m (Figure 12d,e). However, only a small number of source areas could be identified using the 30 m resolution DEM (Figure 12f) [39].
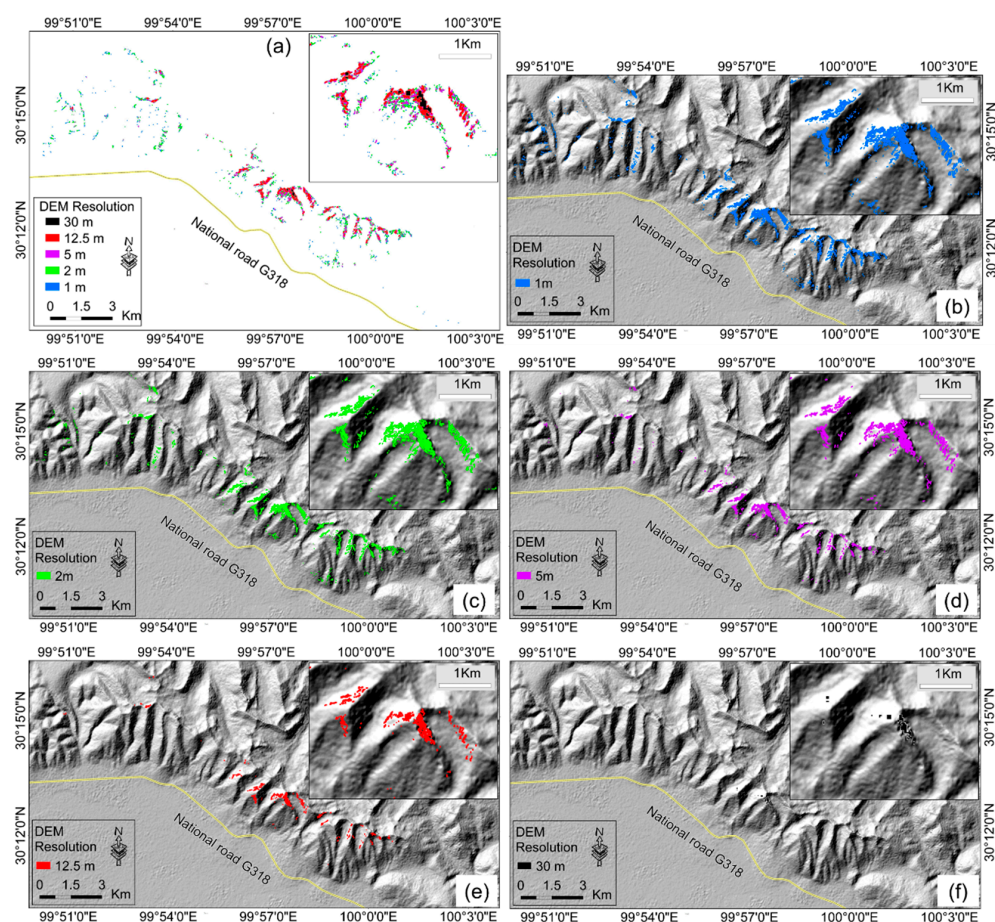

Figure 12. Rockfall source area identification under five different resolutions. (**a**) Overlay map of identification results of five different resolutions; (**b**) 1 m DEM resolution; (**c**) 2 m DEM resolution; (**d**) 5 m DEM resolution; (**e**) 12.5 m DEM resolution; (**f**) 30 m DEM resolution (shaded relief map based on 1 m DEM, accessed through UAV photogrammetry).

Additionally, the size of the NA used to search for the current slope surface relief is also a crucial factor that affects the accuracy of the prediction results [23,40]. If other parameters remain constant, the LSR is a known value. As the NA increases, so does the SSR, which can cause more grids to be incorrectly classified as having lower stability than their actual state (meeting the condition of SSR > LSR) [40]. Therefore, careful selection of the NA value is crucial to achieving effective identification. We conducted calculations using four different NA values to qualitatively compare the influence of NA value on the identification of rockfall source areas (Figure 13). Among them, when the arena value was set to 50 m, only a small portion of the source regions could be identified. Furthermore, when the NA exceeded 200 m, the source regions were significantly over-recognized. Therefore, as a conservative estimate, we defined the NA for searching potential rockfall source areas to be 200 m in this study.
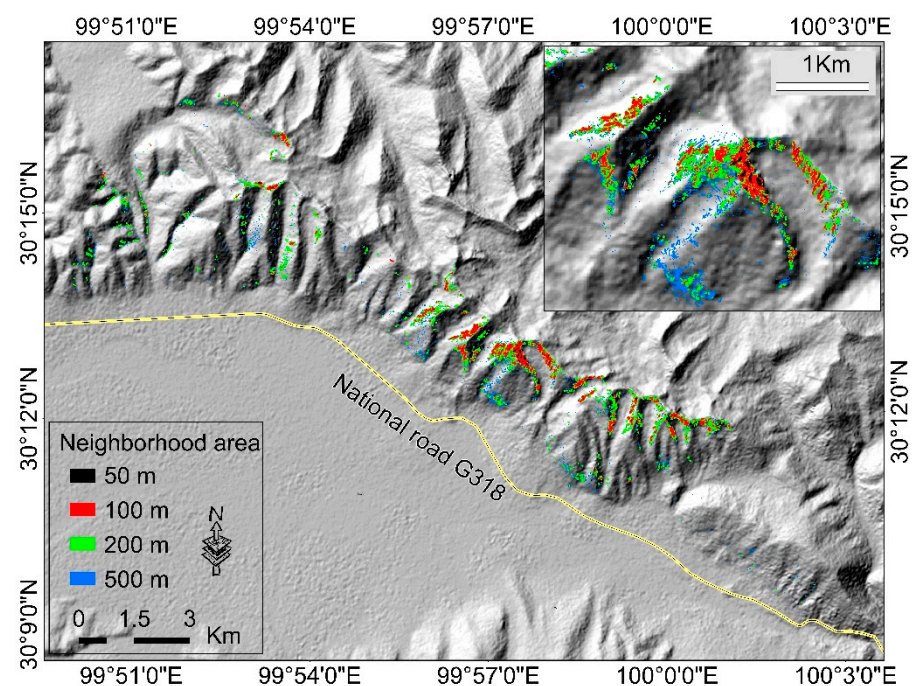

Figure 13. Rockfall source areas identification under four different neighborhood areas (shaded relief map based on 1 m DEM, accessed through UAV photogrammetry).

6. Conclusions

This paper proposed an automatic PRSI procedure based on the ArcGIS framework and Culmann's two-dimensional slope stability model, which enables rapid identification of rockfall source areas at a regional scale. Combining field investigation, high-precision aerial photogrammetry, and numerical simulation, we applied this method to the Maoyaba basin as an example for performing rapid identification and hazard assessment.

(1) We improved the procedure of PRSI in the high mountain areas of the Tibetan Plateau. The PRSI procedure identified 80.85% of rockfall source areas that overlapped with the results from remote sensing images, providing validation for the reliability and effectiveness of our procedure;

(2) The majority of rockfall source areas identified using the PRSI procedure are distributed on slopes with high relief and steep terrain, mostly concentrated in regions with frost weathering zones;

(3) The resolution of the digital elevation model (DEM) plays a crucial role in controlling the accuracy of the identification results. This study found that DEMs with high resolutions (i.e., 1 m and 2 m) and medium resolutions (i.e., 5 m) performed well in identifying rockfall sources. Therefore, this study provides guidance for selecting the most suitable DEM resolution for PRSI;

(4) Conducting PRSI and hazard assessment for these areas can provide effective support for disaster prevention and mitigation efforts. The simulation results showed that some parts of the route are threatened by potential rockfall, indicating that appropriate protective measures should be taken.

Data Availability Statement: The Digital Elevation Model (DEM) and potential rockfall source areas of this study are available from the corresponding author upon request. Contact address: wangxueliang@mail.iggcas.ac.cn.

Conflicts of Interest: The authors declare that they have no known competing financial interest or personal relationships that could have appeared to influence the work reported in this paper.

References

1. Houtian, H. Preliminary investigation on the classification of landfalls. *J. China Railw. Soc.* **1985**, *7*, 90–100.
2. Huang, R.; Liu, W.; Zhou, J.; Pei, X. Experimental field study of movement charateristics of rock blocks falling down a slope. *J. Earth Sci.* **2010**, *21*, 330–339. [CrossRef]
3. Messenzehl, K.; Dikau, R. Structural and thermal controls of rockfall frequency and magnitude within rockwall-talus systems (Swiss Alps). *Earth Surf. Process. Landf.* **2017**, *42*, 1963–1981. [CrossRef]
4. Crosta, G.B.; Agliardi, F. A methodology for physically based rockfall hazard assessment. *Nat. Hazards Earth Syst. Sci.* **2003**, *3*, 407–422. [CrossRef]
5. Fanos, A.M.; Pradhan, B. A Novel Hybrid Machine Learning-Based Model for Rockfall Source Identification in Presence of Other Landslide Types Using LiDAR and GIS. *Earth Syst. Environ.* **2019**, *3*, 491–506. [CrossRef]
6. Wang, X.; Clague, J.J.; Crosta, G.B.; Sun, J.; Stead, D.; Qi, S.; Zhang, L. Relationship between the spatial distribution of landslides and rock mass strength, and implications for the driving mechanism of landslides in tectonically active mountain ranges. *Eng. Geol.* **2021**, *292*, 106281. [CrossRef]
7. Yarahmadi, R.; Bagherpour, R.; Taherian, S.-G.; Sousa, L.M. Discontinuity modelling and rock block geometry identification to optimize production in dimension stone quarries. *Eng. Geol.* **2018**, *232*, 22–33. [CrossRef]
8. Yan, J.; Chen, J.; Tan, C.; Zhang, Y.; Liu, Y.; Zhao, X.; Wang, Q. Rockfall source areas identification at local scale by integrating discontinuity-based threshold slope angle and rockfall trajectory analyses. *Eng. Geol.* **2023**, *313*, 106993. [CrossRef]
9. Molnar, P.; Anderson, R.S.; Anderson, S.P. Tectonics, fracturing of rock, and erosion. *J. Geophys. Res.* **2007**, *112*, 1–12. [CrossRef]
10. Partsinevelos, P.; Kritikakis, G.; Economou, N.; Agioutantis, Z.; Tripolitsiotis, A.; Mertikas, S.; Vafidis, A. Integration of seismic and image data processing for rockfall monitoring and early warning along transportation networks. *Nat. Hazards* **2016**, *83*, 133–153. [CrossRef]
11. Abellán, A.; Calvet, J.; Vilaplana, J.M.; Blanchard, J. Detection and spatial prediction of rockfalls by means of terrestrial laser scanner monitoring. *Geomorphology* **2010**, *119*, 162–171. [CrossRef]
12. Mavrouli, O.; Corominas, J. Comparing rockfall scar volumes and kinematically detachable rock masses. *Eng. Geol.* **2017**, *219*, 64–73. [CrossRef]
13. Zhao, S.; Dai, F.; Deng, J.; Wen, H.; Li, H.; Chen, F. Insights into landslide development and susceptibility in extremely complex alpine geoenvironments along the western Sichuan–Tibet Engineering Corridor, China. *CATENA* **2023**, *227*, 107105. [CrossRef]
14. Wang, X.; Crosta, G.B.; Clague, J.J.; Stead, D.; Sun, J.; Qi, S.; Liu, H. Fault controls on spatial variation of fracture density and rock mass strength within the Yarlung Tsangpo Fault damage zone (southeastern Tibet). *Eng. Geol.* **2021**, *291*, 106238. [CrossRef]
15. Gallo, I.G.; Martínez-Corbella, M.; Sarro, R.; Iovine, G.; López-Vinielles, J.; Hérnandez, M.; Robustelli, G.; Mateos, R.M.; García-Davalillo, J.C. An Integration of UAV-Based Photogrammetry and 3D Modelling for Rockfall Hazard Assessment: The Cárcavos Case in 2018 (Spain). *Remote Sens.* **2021**, *13*, 3450. [CrossRef]
16. Michoud, C.; Derron, M.-H.; Horton, P.; Jaboyedoff, M.; Baillifard, F.-J.; Loye, A.; Nicolet, P.; Pedrazzini, A.; Queyrel, A. Rockfall hazard and risk assessments along roads at a regional scale: Example in Swiss Alps. *Nat. Hazards Earth Syst. Sci.* **2012**, *12*, 615–629. [CrossRef]
17. Lopez-Saez, J.; Corona, C.; Eckert, N.; Stoffel, M.; Bourrier, F.; Berger, F. Impacts of land-use and land-cover changes on rockfall propagation: Insights from the Grenoble conurbation. *Sci. Total Environ.* **2016**, *547*, 345–355. [CrossRef]

18. Zhan, J.; Yu, Z.; Lv, Y.; Peng, J.; Song, S.; Yao, Z. Rockfall Hazard Assessment in the Taihang Grand Canyon Scenic Area Integrating Regional-Scale Identification of Potential Rockfall Sources. *Remote Sens.* **2022**, *14*, 3021. [CrossRef]
19. Agliardi, F.; Riva, F.; Galletti, L.; Zanchi, A.; Crosta, G.B. Rockfall source characterization at high rock walls in complex geological settings by photogrammetry, structural analysis and DFN techniques. *EGU Gen. Assem. Conf. Abstr.* **2016**, *18*, 13071.
20. Moore, J.R.; Sanders, J.W.; Dietrich, W.E.; Glaser, S.D. Influence of rock mass strength on the erosion rate of alpine cliffs. *Earth Surf. Process. Landf.* **2009**, *34*, 1339–1352. [CrossRef]
21. Crosta, G.B.; Utili, S.; de Blasio, F.V.; Castellanza, R. Reassessing rock mass properties and slope instability triggering conditions in Valles Marineris, Mars. *Earth Planet. Sci. Lett.* **2014**, *388*, 329–342. [CrossRef]
22. Bigot-Cormier, F.; Montgomery, D.R. Valles Marineris landslides: Evidence for a strength limit to Martian relief? *Earth Planet. Sci. Lett.* **2007**, *260*, 179–186. [CrossRef]
23. Wang, X.; Liu, H.; Sun, J. A New Approach for Identification of Potential Rockfall Source Areas Controlled by Rock Mass Strength at a Regional Scale. *Remote Sens.* **2021**, *13*, 938. [CrossRef]
24. Matasci, B.; Stock, G.M.; Jaboyedoff, M.; Carrea, D.; Collins, B.D.; Guérin, A.; Matasci, G.; Ravanel, L. Assessing rockfall susceptibility in steep and overhanging slopes using three-dimensional analysis of failure mechanisms. *Landslides* **2018**, *15*, 859–878. [CrossRef]
25. Zhang, W.; Zhao, X.; Pan, X.; Wei, M.; Yan, J.; Chen, J. Characterization of high and steep slopes and 3D rockfall statistical kinematic analysis for Kangyuqu area, China. *Eng. Geol.* **2022**, *308*, 106807. [CrossRef]
26. Liu, H.; Wang, X.; Liao, X.; Sun, J.; Zhang, S. Rockfall Investigation and Hazard Assessment from Nang County to Jiacha County in Tibet. *Appl. Sci.* **2020**, *10*, 247. [CrossRef]
27. James, M.R.; Robson, S.; d'Oleire-Oltmanns, S.; Niethammer, U. Optimising UAV topographic surveys processed with structure-from-motion: Ground control quality, quantity and bundle adjustment. *Geomorphology* **2017**, *280*, 51–66. [CrossRef]
28. Wang, X.; Frattini, P.; Stead, D.; Sun, J.; Liu, H.; Valagussa, A.; Li, L. Dynamic rockfall risk analysis. *Eng. Geol.* **2020**, *272*, 105622. [CrossRef]
29. Sun, J.; Wang, X.; Liu, H.; Yuan, H. Effects of the attitude of dominant joints on the mobility of translational landslides. *Landslides* **2021**, *18*, 2483–2498. [CrossRef]
30. Schmidt, K.M. Limits to Relief. *Science* **1995**, *270*, 617–620. [CrossRef]
31. DiBiase, R.A.; Rossi, M.W.; Neely, A.B. Fracture density and grain size controls on the relief structure of bedrock landscapes. *Geology* **2018**, *46*, 399–402. [CrossRef]
32. Agliardi, F.; Crosta, G.B.; Meloni, F.; Valle, C.; Rivolta, C. Structurally-controlled instability, damage and slope failure in a porphyry rock mass. *Tectonophysics* **2013**, *605*, 34–47. [CrossRef]
33. Xiuli, W.; Yonghong, R.; Junjie, L. analysis of shock resistance of new debris flow dam with continuous crash bearers. *J. Disaster Prev. Mitig. Eng.* **2017**, *37*, 474–480.
34. Jie, S.; Cheng, Z.; Shengshui, C. Numerical simulation of flexible gabion arch dam to prevent and control debris flow blocks. *Chin. J. Geotech. Eng.* **2015**, *37*, 269–275.
35. Di, Z.; Jiacun, L.; Zhonghai, W.; Shaotang, L.; Yan, L. Using terrestrial LiDAR to accurately measure the microgeomorphologic geometry of active fault: A case study of fault scarp on the Maoyaba fault zone. *J. Geomech.* **2021**, *27*, 63–72.
36. Zeng, Q.; Zhang, L.; Davies, T.; Yuan, G.; Xue, X.; Wei, R.; Yin, Q.; Liao, L. Morphology and inner structure of Luanshibao rock avalanche in Litang, China and its implications for long-runout mechanisms. *Eng. Geol.* **2019**, *260*, 105216. [CrossRef]
37. Qiu, H.; Zhu, Y.; Zhou, W.; Sun, H.; He, J.; Liu, Z. Influence of DEM resolution on landslide simulation performance based on the Scoops3D model. *Geomat. Nat. Hazards Risk* **2022**, *13*, 1663–1681. [CrossRef]
38. Loye, A.; Jaboyedoff, M.; Pedrazzini, A. Identification of potential rockfall source areas at a regional scale using a DEM-based geomorphometric analysis. *Nat. Hazards Earth Syst. Sci.* **2009**, *9*, 1643–1653. [CrossRef]
39. Viotto, S.; Toyos, G.; Bookhagen, B. An assessment of the effects of DEM quality and spatial resolution on a model for mapping lahar inundation areas at volcán Copahue (Argentina & Chile). *J. South Am. Earth Sci.* **2023**, *121*, 104138. [CrossRef]
40. Russell, E.; Padró, J.-C.; Montero, P.; Domingo-Marimon, C.; Carabassa, V. Relief Modeling in the Restoration of Extractive Activities Using Drone Imagery. *Sensors* **2023**, *23*, 2097. [CrossRef]